

# Nanoscale

Accepted Manuscript

This article can be cited before page numbers have been issued, to do this please use: M. Moglianetti, M. Gamón Rodríguez, R. Lamuraglia, E. Galvagno, S. Marras, S. Dante, R. Brescia, A. Carmignani, M. Battaglini, G. Ciofani, F. Menegazzo and A. Traviglia, *Nanoscale*, 2025, DOI: 10.1039/D5NR02680F.



This is an Accepted Manuscript, which has been through the Royal Society of Chemistry peer review process and has been accepted for publication.

Accepted Manuscripts are published online shortly after acceptance, before technical editing, formatting and proof reading. Using this free service, authors can make their results available to the community, in citable form, before we publish the edited article. We will replace this Accepted Manuscript with the edited and formatted Advance Article as soon as it is available.

You can find more information about Accepted Manuscripts in the [Information for Authors](#).

Please note that technical editing may introduce minor changes to the text and/or graphics, which may alter content. The journal's standard [Terms & Conditions](#) and the [Ethical guidelines](#) still apply. In no event shall the Royal Society of Chemistry be held responsible for any errors or omissions in this Accepted Manuscript or any consequences arising from the use of any information it contains.

## ARTICLE

# Engineering Ultra-small Nanocerium with Antioxidant and UV-shielding Properties as Functional Nanomaterials in Composite Coatings for Complex Surface Protection

Erica Galvagno<sup>a,b</sup>, Sergio Marras<sup>c</sup>, Silvia Dante<sup>c</sup>, Rosaria Brescia<sup>d</sup>, Miquel Gamón Rodríguez<sup>e</sup>, Alessio Carmignani<sup>f</sup>, Matteo Battaglini<sup>f</sup>, Gianni Ciofani<sup>f</sup>, Raffaella Lamuraglia<sup>a</sup>, Federica Menegazzo<sup>b</sup>, Arianna Traviglia<sup>a\*</sup>, and Mauro Moglianetti<sup>a\*</sup>

Received 00th January 20xx,  
Accepted 00th January 20xx

DOI: 10.1039/x0xx00000x

The development of advanced catalytic shields against UV-induced and oxidative degradation phenomena is critical to address multifaceted deterioration processes. The maximization of the surface-to-volume ratio in ultra-small cerium oxide nanoparticles (CeO<sub>2</sub> NPs) favors the Ce(III)/Ce(IV) exchange on the surface and the formation of oxygen vacancies, creating the ideal platform to target entangled degradation issues. Here, we design a microwave-assisted scalable process to obtain highly stable CeO<sub>2</sub> NPs (2 nm), and we demonstrate the redox cycling of the nanocatalyst by means of Environmental XPS. Thereafter, we develop a polymer nanocomposite formulation in which the biopolymer and the catalytic nanomaterial work synergistically to provide a protective action without hindering the active sites present at the surface of the NPs. We test the protective action of the coating in the challenging context of cultural heritage, investigating its performance on ancient frescoes. Their surfaces are often subjected to pigment degradation, triggered by a combination of light, salts, and high relative humidity. We verify how, thanks to the joint action of the biopolymer and the NPs, the CeO<sub>2</sub> NPs-based coating effectively mitigates complex deterioration mechanisms.

## Introduction

Functional nanomaterials represent a highly promising domain for creating advanced catalytic shields capable of mitigating complex deterioration pathways triggered by UV exposure and oxidative species. Cerium oxide nanoparticles (CeO<sub>2</sub> NPs) emerge as ideal candidates to simultaneously overcome both challenges, owing to their dual antioxidant and UV-shielding functionalities. Their versatility arises from the formation of oxygen vacancies and the efficient Ce(III)/Ce(IV) redox cycling at the surface.<sup>1–5</sup> However, despite their great potential, their application as functional components of protective coatings remains limited, especially in the protection of painted surfaces and cementitious structures.<sup>5–8</sup> To date, scientific efforts have predominantly focused on using CeO<sub>2</sub> NPs in coatings designed for metal corrosion protection, while UV-shielding and anti-

ageing coatings have only been marginally explored.<sup>8–12</sup> Furthermore, their UV-shielding properties have been used to slow down the ageing process of polymeric matrixes, overlooking their potential in the protection of the underlying substrate.<sup>9,13</sup> Several limitations have emerged in recent coating applications and novel strategies are needed to overcome them. First, it is crucial to rigorously define the function of the NPs within complex multicomponent systems. Indeed, an insufficient evaluation can compromise the design of accurately engineered strategies.<sup>9–11,13,14</sup> Additionally, investigations should aim at optimized integration of the NPs into polymeric and epoxy matrixes. The focus on this key point allows to overcome issues related to aggregation phenomena, which can severely diminish catalytic efficiency and reduce optical transparency.<sup>13,15,16</sup>

To address these issues, it is important to enhance the efficiency of NPs and preserve their protective function within the polymeric matrix.<sup>17</sup> First, by producing ultra-small stable NPs, superior performances can be accomplished thanks to the increase in the surface-to-volume ratio.<sup>18–21</sup> Studies in the literature on 3 nm CeO<sub>2</sub> NPs highlight challenges in achieving sufficient stabilization in solution, leading to partial aggregation and, hence, loss of function.<sup>22–25</sup> It is fundamental to overcome this issue and define how the ultra-small size can influence the catalytic activity of the NPs compared to the larger NPs reported in the majority of studies.<sup>26–28</sup> Moreover, the design of the polymer nanocomposite has to be accurately engineered to ensure a strong synergistic interaction between the NPs and the polymeric matrix. Due to their combined action, the coating can

<sup>a</sup> Center for Cultural Heritage Technology CCHT, Istituto Italiano di Tecnologia (IIT), Via A. Olivetti 1, Roncade (TV), 31056, Italy.

<sup>b</sup> Dipartimento di Scienze Molecolari e Nanosistemi, Università Ca' Foscari di Venezia, Via Torino 155, Venezia Mestre, 30172, Italy.

<sup>c</sup> Materials characterization Facility, Istituto Italiano di Tecnologia (IIT), Via Morego 30, 16163 Genova, Italy.

<sup>d</sup> Electron Microscopy Facility, Istituto Italiano di Tecnologia (IIT), Via Morego 30, 16163 Genova, Italy.

<sup>e</sup> Department of Surface and Plasma Science, Faculty of Mathematics and Physics, Charles University, V Holešovičkách 2, 180 00 Praha 8, Czech Republic

<sup>f</sup> Smart Bio-Interfaces, Istituto Italiano di Tecnologia, 56025 Pontedera, Italy

Supplementary Information available: [details of any supplementary information available should be included here]. See DOI: 10.1039/x0xx00000x



reliably perform even in the most challenging conditions. To provide incontrovertible proof of this premise, we sought to identify the most complex type of surface to test the coating's ability to prevent irreversible changes. The field of cultural heritage conservation responds to this need and ancient frescoes constitute a solid case study to test degradation in outdoor environments. In this specific context, darkening processes have been observed for several pigments, with cinnabar being an emblematic example.<sup>29–34</sup> Given the system's complexity, current conservation strategies have proven insufficient in effectively mitigating pigment degradation. Instead, the field predominantly relies on the use of synthetic polymers or resins.<sup>35–40</sup> Additionally, in the last two decades, NPs with specific functions have emerged as promising strategies, but none of them appears to have the required properties to tackle the issue of color change in frescoes, which often involves both UV-induced phenomena and redox mechanisms.<sup>41–53</sup> The strict requirements of the field add a degree of complexity to the formulation of innovative protective strategies. Indeed, artworks require far more sophisticated conservation approaches than any contemporary material. In particular, the field of cultural heritage conservation demands a precise set of characteristics for any protective product. To this aim, the coating should present a delicate combination of transparency, water vapor permeability, long-lasting efficacy, and efficient barrier effect.<sup>35,54,55</sup>

In this work, we have produced ultra-small CeO<sub>2</sub> NPs aiming at maximizing the surface-to-volume ratio and, simultaneously, improving the catalytic performances by favoring the Ce(III)/Ce(IV) conversion at the surface. We have established a well-defined structure-function relationship and ascertained the response of the NPs to the interaction with different environmental factors (*i.e.*, light, oxygen-based species, and high temperature). Furthermore, we have developed a chitosan formulation to evenly distribute the NPs on the substrates and provide extensive protection thanks to its barrier effect and filming properties.<sup>56</sup> Lastly, we tested the coating against the degradation of cinnabar (HgS) in frescoes, a critical process caused by the simultaneous presence of light, salts, and high relative humidity. We have demonstrated that the synergy between the polymeric matrix and the catalytic properties of the NPs slows down or even halts the deterioration of cinnabar, paving the way to its cross-field applications.

## Results and discussion

### Synthesis and characterization of CeO<sub>2</sub> NPs.

The development of nanomaterials with enhanced catalytic activity is a critical step to produce efficient, effective, and sustainable systems with optimal performances. To achieve this task, we focused on strategies to maximize the surface-to-volume ratio with the final aim of increasing the number of

available active sites on the surface per given mass of NPs. Indeed, size is a decisive factor as it affects the extent of surface that results available for the catalytic activity. For this reason, we designed and scaled up a synthetic protocol to produce ultra-small CeO<sub>2</sub> NPs, leveraging on a recently published hydrothermal protocol.<sup>57</sup> The synthesis is performed in aqueous environment and the NPs are stabilized with sodium citrate. This capping agent improves the stability of the NPs in the dispersion, by avoiding aggregation phenomena. Contrarily to the published synthesis, we implemented a microwave-assisted protocol, and we tested both tetramethylammonium hydroxide, TMAOH, and ammonium hydroxide, NH<sub>4</sub>OH, to create the required alkaline environment. In this section, we compared the characteristics of the resulting NPs, named t-NPs and a-NPs, respectively.

The XRD pattern of the a-NPs is in agreement with the expected fluorite structure (space group *Fm3m*(225)), confirming the formation of crystalline cubic CeO<sub>2</sub> NPs (**Figure 1a**). Size analysis from XRD data establishes that the average diameter of the NPs in powder form is equal to  $3.18 \pm 0.06$  nm. This data is representative of the whole sample, but it could be affected by aggregation phenomena established during the freeze-drying process implemented to dry the NPs. Therefore, TEM and SAXS analyses were also performed, and they prove that ultra-small citrate-capped NPs were synthesized. From the analysis of the TEM images reported in **Figure 1b** and Figure S1a, an average diameter of  $2.2 \pm 0.4$  nm was calculated for a-NPs. t-NPs present a similar size distribution centered at  $2.1 \pm 0.4$  nm (Figure S1b). In both cases, the size is homogeneous throughout the portion of NPs analyzed, and the NPs are well-separated despite the potential influence of solvent evaporation on their aggregation. We achieved a polydispersity of about 18.2%; this result is in line with recently published reports and is satisfactory considering the ultra-small dimension of the NPs.<sup>57</sup> However, BF-TEM size analysis is based on a limited number of NPs and in dry conditions. Therefore, to test the aggregation state and the stability in aqueous environments and to account for a larger number of NPs, we performed SAXS measurements (**Figure 1d** and Figure S2a), which also provide valuable information on the hydration shell and the stabilizing agents. The size distribution by volume shows that a-NPs have an average radius of  $1.9 \pm 0.7$  nm, while the average radius of t-NPs has been determined to be about  $1.3 \pm 0.3$  nm for t-NPs (**Figure 1e** and Figure S2b respectively). Most probably, the discrepancy between TEM and SAXS is due to the limits of TEM analysis, which does not allow to detect the hydration shell and the thin organic coating around the NPs. Nevertheless, SAXS analysis confirms that NPs do not aggregate, even considering a vast number of NPs. This result is highly relevant for the application of the NPs in different fields as the absence of aggregation guarantees that all the surface area is available for the catalytic activity. Additionally, SAXS measurements were repeated after 6 months from the preparation of the synthesis and the same average radius has been determined both for a-NPs and t-NPs, within the experimental uncertainty (Figure S2c-f). This advanced characterization demonstrates that we have achieved significant stability of the NPs in aqueous dispersion, an



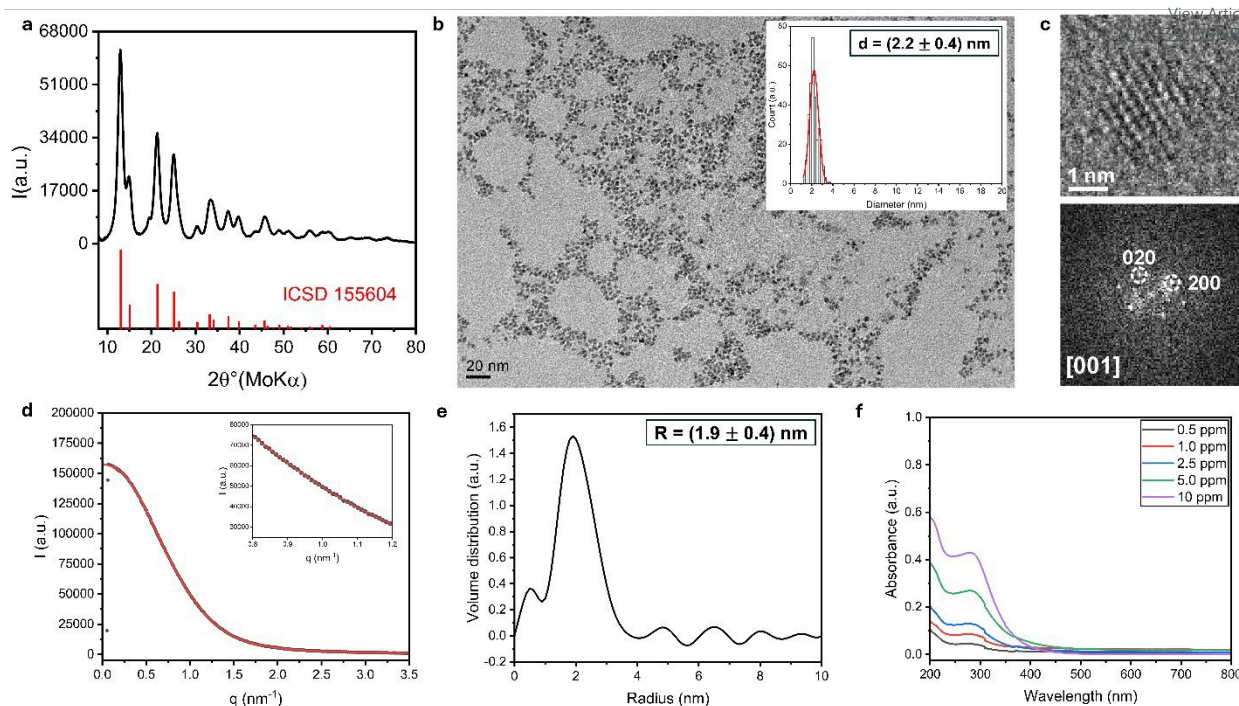


Figure 1. **a**, XRD pattern of CeO<sub>2</sub> NPs with corresponding reference peaks. **b**, BF-TEM image of a-NPs with the corresponding size distribution (insert). **c**, HRTEM image and corresponding FFT of an individual a-NP, indexed based on cubic CeO<sub>2</sub> (ICSD 155604). **d**, Experimental curve (black dots) and fit (red line) of SAXS data of a-NPs (in the insert: zoomed-in portion of the graph). **e**, Size distribution by volume of a-NPs, obtained from SAXS measurements. **f**, UV-visible spectrum of a-NPs at different concentrations.

important factor for their effective use in long-term applications. Furthermore, the ultra-small size achieved with this scale-up protocol is pivotal because it leads to maximizing the surface-to-volume ratio, hence, to a marked increase in the number of available active sites on the surface.

To further study the surface structure of the NPs, HRTEM was employed since it provides information on the shape and the crystal structure at the nm scale. As can be observed in **Figure 1c** and in **Figure S1c**, both a-NPs and t-NPs are isotropic (*i.e.*, they are not enclosed by extended facets). Strain analysis on XRD data confirms this observation. Crystal strain is estimated to be of  $0.78 \pm 0.06\%$  with a refined lattice parameter of  $5.434 \pm 0.004 \text{ \AA}$ . Lattice strain is generally correlated to the formation of defects which, in CeO<sub>2</sub> NPs, mainly correspond to the formation of oxygen vacancies.<sup>58</sup> In particular, strain is expected in ultra-small NPs due to the high concentration of Ce(III) on the surface; furthermore, the surface takes on a major role due to the increased surface-to-volume ratio.<sup>59</sup>

The presence of Ce(III) and Ce(IV) ions in CeO<sub>2</sub> NPs can be determined through UV-visible spectroscopy. The trivalent cation generally absorbs in the range 230 – 270 nm, while the absorbance of Ce(IV) falls at higher wavelengths, 300 – 400 nm.<sup>60,61</sup> As shown in **Figure 1f** and **Figure S3**, the spectra of a-NPs and t-NPs have both characteristic bands, indicating the simultaneous presence of both oxidation states in the NPs. Nevertheless, precise quantification is quite complex with this technique because the characteristic peaks are partially superimposed, and the simultaneous presence of both oxidation states could only be determined in solution.

The relative ratio Ce(III)/Ce(IV) was deeply investigated through Environmental XPS in order to confirm the highly substoichiometric character of the NPs and gather quantitative information. The XPS characterization was focused on Ce 3d peaks, which include both Ce(III)- and Ce(IV)-related signals. In particular, U-type peaks are related to 3d<sub>3/2</sub>, while V ones are related to 3d<sub>5/2</sub>. V<sub>0</sub>, V', U<sub>0</sub>, and U' (880.9, 885.2, 899.1, and 903.4 eV) represent Ce<sup>3+</sup> species, while V, V'', V''', U, U'', and U''' (882.7, 888.5, 898.3, 901.3, 907.3, and 916.9 eV) are characteristic of Ce<sup>4+</sup> species.<sup>62,63</sup> All analyzed samples present a mixed valence state while having a slightly higher percentage of Ce<sup>4+</sup>. In a-NPs, Ce<sup>3+</sup> amounts to 46.3%, when the measurement is performed in an Ar atmosphere (**Figure 2a**). Similar values were obtained for t-NPs, where Ce(III) amounts to 41.9% (**Figure S4**). These results agree with previous observations regarding crystal strain in ultra-small CeO<sub>2</sub> NPs. Considering that a-NPs and t-NPs do not present significant differences in terms of physico-chemical properties and catalytic activity (as described in **Figure S5a** and **S5b**), the following investigations will be focused on a-NPs, due to the advantages we mentioned related to the use of NH<sub>4</sub>OH.

### Redox cycling and related catalytic activity of CeO<sub>2</sub> NPs.

In order to establish a clear structure-function relationship in the NPs, the physico-chemical characteristics need to be correlated to the redox cycling that can be established on the surface of the NPs. Indeed, the reversible conversion between Ce(III) and Ce(IV) is linked not only to crystal strain and the ultra-





small size of the NPs, but also to the catalytic properties. For this reason, we deepened the characterization by investigating how

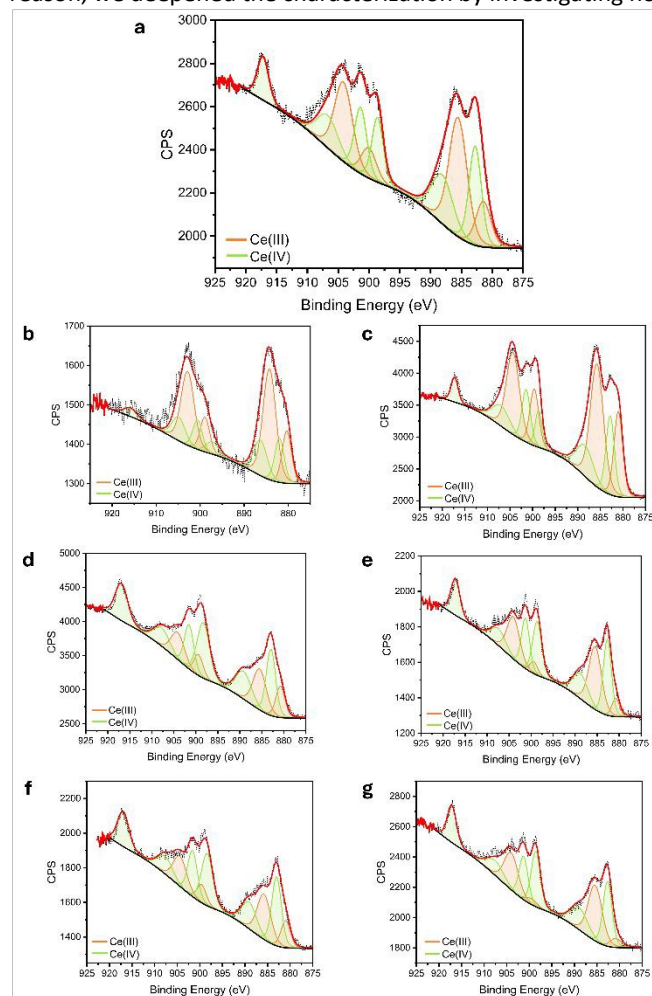


Figure 3. Ce 3d region of a-NPs where Ce(III) (orange) and Ce(IV) (green) have been fitted. The measurements were acquired for the NPs deposited and dried on silicon wafer in the following conditions. **a**, In an Ar atmosphere. **b**, In an Ar atmosphere after 3 months of exposure to natural light. **c**, In an Ar atmosphere, after heating the NPs to 300°C on a button heater. **d**, In an O<sub>2</sub> atmosphere. **e**, In an Ar atmosphere after adding H<sub>2</sub>O<sub>2</sub> (H<sub>2</sub>O<sub>2</sub>/NPs ratio: 1:2). **e**, **g**, Ce 3d region of a-NPs acquired in solution with an ad hoc engineered cell system; image **g** shows the spectrum of the NPs in solution with H<sub>2</sub>O<sub>2</sub>.

the Ce(III)/Ce(IV) ratio changes when the nanocatalyst is subjected to different factors.

This study leverages on the unique features of Environmental XPS, which provides information on the samples analyzed in conditions similar to the environmental ones. Indeed, the acquisition is not performed at a high vacuum. Instead, the measurements are collected at a pressure that is closer to the atmospheric one compared to standard instruments, allowing us to gain information on the sample in solution. In this work, the main parameters under investigation are light, high temperature (300°C), an O<sub>2</sub> atmosphere (as opposed to the conventional Ar atmosphere), and H<sub>2</sub>O<sub>2</sub>. Light exposure leads to an increase in the percentage of Ce<sup>3+</sup> to 64.9% (Figure 2b), while a significant temperature increase induces a rise to 62.2% (Figure 2c). Differently, the NPs that were studied in an O<sub>2</sub> atmosphere show the opposite trend. In the O<sub>2</sub> atmosphere the percentage of Ce<sup>3+</sup> in the deposited NPs diminishes to 32.2%

(Figure 2d) and the same effect can be observed when the measurement is performed in an ultrapure water solution (decrease to 38.9%, Figure 2e). This shows the dependence of the Ce(III)/Ce(IV) ratio on the environmental conditions, which can be both reducing (*i.e.*, light and temperature increase) and oxidizing (*i.e.*, O<sub>2</sub> influence). Consequently, the starting Ce(III)/Ce(IV) ratio can be restored simply by interacting with commonly present environmental factors. This observation allows us to further comment on the regeneration potential of the nanocatalyst. Indeed, its performance in catalytic applications is strongly connected to the stoichiometry of Ce atoms at the surface of the NPs.<sup>64,65</sup> The activity is influenced by the presence of Ce(III) and the formation of surface defects in the form of oxygen vacancies.<sup>66</sup> Consequently, the regeneration potential of the nanocatalyst due to the opposite effects of different environmental factors opens the way to long-term efficiency of its protective action.

In the specific case of the oxygen-related activity of the NPs, the catalytic activity resembles an enzyme-like behavior with CeO<sub>2</sub> NPs presenting both peroxidase- and oxidase-like activity. In the first case, the NPs can decompose H<sub>2</sub>O<sub>2</sub> to finally produce water, while in the second case, the NPs interact with O<sub>2</sub> to generate either H<sub>2</sub>O<sub>2</sub> or H<sub>2</sub>O. Considering this activity and how it could be exploited to exert a protective action in the coating, we investigated how the interaction with both species can influence the Ce(III)/Ce(IV) ratio. As discussed, an O<sub>2</sub> atmosphere and an ultrapure water solution can have an oxidizing effect on the NPs, decreasing the amount of Ce(III). Additionally, we used Environmental XPS to study how the Ce(III)/Ce(IV) ratio changes when the NPs interact with H<sub>2</sub>O<sub>2</sub>. First, the measurements were performed after adding H<sub>2</sub>O<sub>2</sub> to the NPs which were previously deposited and dried on a silicon wafer. Then, tests were repeated in an aqueous solution containing H<sub>2</sub>O<sub>2</sub>. In both cases, the Ce<sup>3+</sup> percentage decreases to 34.3% for the deposited NPs (Figure 2f) and to 37.5% in solution (Figure 2g). We have then expanded on these results by assessing the peroxidase- and oxidase-like activity of the NPs. This investigation allows to determine the effect of the NPs on oxygen-based species and provides information on the concentration at which the NPs are active, and the time needed to observe an effect.

The tetramethylbenzidine (TMB) assay was employed to test the performance of different concentrations of the NPs, and the results are reported in Figure 3a and 3b. The optimal reaction

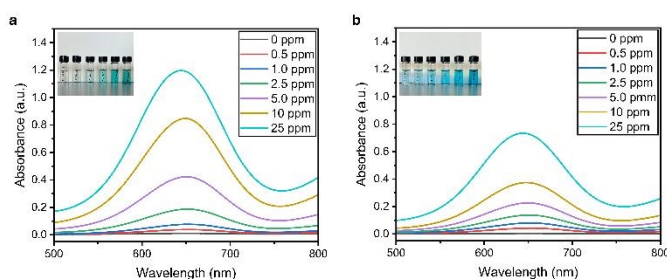


Figure 2. **a**, Peroxidase-like activity of a-NPs determined in an ultrapure water solution by studying its interaction with H<sub>2</sub>O<sub>2</sub> in the presence of TMB. **b**, Oxidase-like activity of a-NPs determined in an ultrapure water solution by studying its interaction with O<sub>2</sub> in the presence of TMB.



time was chosen by evaluating the onset of the plateau region at which maximum concentration of the oxidized form of TMB is reached. Measurements were performed at different NPs concentrations, ranging from 0.5 to 25 ppm, proving that the minimum concentration at which a signal can be detected is 1 ppm. The result is in agreement with the ultra-small size of the NPs, which provides them with a larger surface area for the catalytic activity.

### Biocompatibility assessment.

The formulation of a coating based on CeO<sub>2</sub> NPs needs to take into account any health and safety concerns that the components of the coating might pose. In the case of the formulation proposed in this work, chitosan has been selected as a sustainable and biocompatible matrix. Its biodegradability and recognized safety make it an optimal alternative to formulate biocompatible coatings.<sup>67–70</sup> Instead, the potential toxicity of CeO<sub>2</sub> NPs should be explored. Indeed, considering the ultra-small dimension and the enzyme-like activity of the NPs, it is fundamental to investigate how these properties can impact the interaction with cells, since a decrease in NPs size and a strong reactivity can alter their biocompatibility profile by impairing cellular metabolism. Taking into account these facts, we performed cell viability assays on a-NPs and t-NPs, to confirm they can be used without health concerns, in alignment with the "Safe by Design" approach. Given the critical role of the NPs' biological identity,<sup>71</sup> we first focused on the influence of the proteins-NPs interaction on the physico-chemical properties and stability of the NPs, which substantially affect their biological identity within cellular systems. We incubated the NPs in a FBS-rich aqueous solution to form a protein coating around them and measured the hydrodynamic diameter. The interaction with proteins leads to a 10-fold increase in the size of the NPs-protein conjugates, as depicted in Figure S6a and S6b. Furthermore, we assessed the changes in the average hydrodynamic diameter of the NPs after incubation in the cell culture medium, in which high ionic strength and high protein concentration are simultaneously present; the diameter was measured at different time points from few minutes to 72 hours. These results demonstrate that, after a slight decrease in the first 24 hours, the hydrodynamic diameter of a-NPs remains constant for up to 72 hours (Figure 4a and 4b). These data demonstrate that a-NPs have good stability in the cell culture medium and that there are no signs of aggregation phenomena. To establish a comparison with previous stability assessments, present in the literature, we measure the changes in the hydrodynamic diameters of two commercial CeO<sub>2</sub> NPs that remain unchanged or slightly increase in the 72 hours (Figure 4a and 4b).

After this evaluation, the *in vitro* cytotoxicity of CeO<sub>2</sub> NPs has been investigated with two different methods: the PicoGreen assay and the LIVE/DEAD assay. The PicoGreen assay has been performed at 24 and 72 hours of NPs incubation. As shown in Figure 4c and Figure S7, the fluorescence signal does not change significantly at either exposure times, indicating that the NPs do not exert significant cytotoxic activity even at concentrations of

100 ppm. We confirmed these results with LIVE/DEAD Assay, which further demonstrates a cell viability of almost 100% after 72 hours of treatment for all the tested NPs concentrations (Figure 4d and 4e). These results are in line with previous assessments on the biocompatibility of CeO<sub>2</sub> NPs.<sup>72,73</sup>

To further establish the influence of NPs size in the interaction with cell membranes and internalization pathways, we have performed internalization tests by means of ICP-MS. The treated cells have a concentration of about  $1.03 \times 10^{-8}$  ng, indicating a very modest internalization compared to what has been observed in the literature for larger CeO<sub>2</sub> NPs (commercial, >25 nm, and synthesized, 8 nm).<sup>72,73</sup> This result represents an important observation and requires further in-depth investigation. Indeed, the exceptional stability of the NPs could possibly reduce their tendency to accumulate within cellular systems, thereby allowing continuous transfer in and out of the cells and avoiding the blockage of intracellular pathways. Moreover, a different factor affecting the uptake is possibly the protein adsorption on the surface of the NPs, which might be disfavored due to their small size.<sup>74</sup> Indeed, the formation of a stable protein corona is generally hindered in ultra-small NPs due to their dimensions and this issue can affect

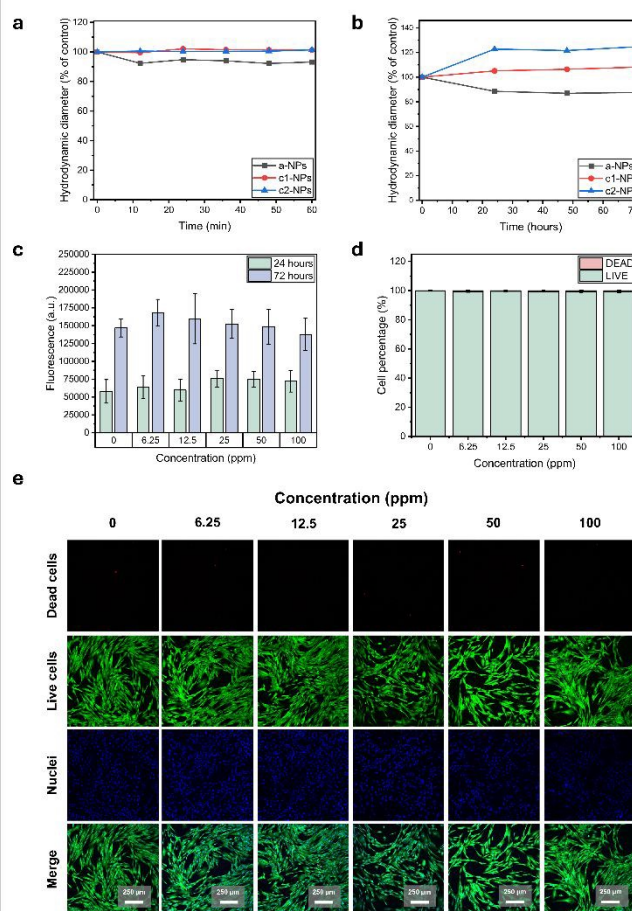


Figure 4. **a,b**, Short- and long-term stability assay of a-NPs and two types of commercial CeO<sub>2</sub> NPs. **c**, PicoGreen assay of a-NPs at two different exposure times, 24 and 72 hours. **d**, Quantitative analysis of data obtained through the LIVE/DEAD cell viability assay. **e**, Representative confocal images of Primary Normal Human Dermal Fibroblasts cells acquired during LIVE/DEAD cell viability assay.



the interaction with cells since the citrate coating could remain as the sole surface functionalization of the NPs. It has been demonstrated by Eppe *et al.* that the presence of carboxylic groups as end groups at the surface has been proven to strongly limit the uptake in cells.<sup>74</sup> Therefore, considering these observations regarding the role of the NPs' surface properties, the carboxyl groups of citrate stabilizing  $\alpha$ -NPs could play a major role in limiting the internalization within cells.

### Design and performance evaluation of the composite coating.

Thanks to their high catalytic activity and potential for long-term protection, the NPs show promising features for the application in multifunctional protective coatings in which they can provide both antioxidant and UV-shielding actions. Furthermore, we confirmed their biocompatibility, which makes them safe both for human health and for the environment. Nevertheless, NPs alone cannot be used as coatings because large quantities would be needed to completely cover the surface and the nanometric size would cause penetration in the highly porous substrates. In order to provide surface protection, the NPs need to remain catalytically active at the surface to shield the substrate from different environmental agents and counteract potentially damaging mechanisms. This poses a particular challenge in the case of porous substrates where it is inevitable for ultra-small NPs in aqueous dispersions to penetrate deep within the structure. For these reasons, the NPs should ideally be included in a filming matrix, such as a polymeric formulation. However, it is fundamental for the composite system not to hinder the catalytic activity of the NPs which act as the functional part of the protective formulation. In this work, we decided to introduce  $\text{CeO}_2$  NPs in a chitosan formulation to form a composite material. We selected chitosan as it provides barrier effect and filming properties whilst being overall more sustainable than conventionally used synthetic polymers. Recently,  $\text{CeO}_2$  NPs and chitosan have been explored to produce composite films for food packaging and wound dressing applications. The publications on the topic impact different fields and show that the synergy between the NPs and the polymeric matrix can lead to multifunctional composites.<sup>75–77</sup> These early works focus on the thermal and mechanical properties of the films, while only marginally exploring antioxidant and antimicrobial properties. Considering the aim of our work, we plan to move the focus on surface characterization and protective capability of the polymer nanocomposite, exploring a novel application for this composite. The concentration of polymer in this formulation is crucial as it imparts specific rheological characteristics, which can in turn affect the filming properties of the substrate and the ease of application.

Leveraging on previous results,<sup>56</sup> we tested chitosan formulations with a chitosan concentration of 0.2% w/V (cs02), 0.4% w/V (cs04), 1.0 % w/V (cs1) and 2.0% w/V (cs2). As depicted in the SEM images reported in Figure S8a-d, the increase in chitosan concentration does not significantly change the morphology of the coating; however, cs2 shows some

fibrous portions which were not visible in the other samples. In terms of rheological properties, the viscosity of all formulations increases compared to cs02 (Table S1). These considerations are important to determine the most suitable application method to apply the coating on the substrate. Given the high viscosity of formulations cs04, cs1, and cs2, we decided to use brush application rather than spray coating. Indeed, high viscosity of the coating would lead to longer application times in the case of spray coating and a viscous formulation could even clog the millimetric nozzle of the airbrush.

All the coatings were applied to fresco mock-ups, which require tailored strategies due to their complexity and to the intricate degradation processes they are subjected to. Indeed, these substrates are highly porous and multilayered, and they comprise both a mortar portion, mostly constituted of  $\text{CaCO}_3$ , and a painted plaster layer. The coating aims at protecting the outer layer, which consists of an inorganic pigment bonded to the surface through carbonation of the plaster beneath. While protection is the main goal of this coating, it is also important to avoid any modification to the aesthetic features of the mock-ups and to preserve water vapor permeability as much as possible.<sup>78,79</sup>

Considering this important point, the aesthetic features of the mock-ups were first monitored after the application of the coating. Table S2 shows the morphology and the color variation (*i.e.*,  $\Delta E$  value) of the samples before and after the application of the coating. We did not measure significant color change even at high concentrations of chitosan, as the index always remained lower than 3 (the value below which the chromatic variation cannot be perceived by naked eye).<sup>80</sup> By achieving significantly low  $\Delta E$  values, we can confirm the transparency of our coating. Additionally, we studied the morphology of the surface through stereomicroscopy (Table S2). The microscopic images of the coated mock-ups confirmed that the morphology of the surface remains unaffected after the application of the coating.

In terms of hydrophobicity, the contact angle was evaluated, and the results are reported in Table S3. The uncoated sample is highly porous and immediately absorbs the water drop. Contrarily, the contact angle falls in the range 40° – 55° for all coated samples and a slight increase can be observed with higher concentrations of chitosan in the formulation. The higher value of contact angle compared to the uncoated sample indicates a more pronounced hydrophobicity of the coating, but the result could also be correlated to changes in the porosity of the surface layers. Indeed, when applying the coating, the pores closer to the surface might be partially clogged by the polymer forming a film over the substrate. In order to quantitatively evaluate this effect, the protection factor and the water vapor permeability have also been determined. On the one hand, the protection factor defines the capability of the substrate of absorbing water up to maximum capacity and is generally used to express the protective performance of the coating. In our specific case, this parameter increases from the uncoated mock-up to the coated ones and reaches the best results for cs1 (Figure 5a). On the other hand, water vapor permeability is generally assessed by determining the water vapor resistance





coefficient. This parameter should ideally be as close as possible to the one determined for the uncoated sample. High permeability of the coating is needed to avoid trapping stagnant water inside the treated substrate as it might lead to structural integrity issues in the long run. As shown in **Figure 5b**, all the coatings we have produced have a slightly lower permeation compared to the uncoated sample and the coefficients gradually decrease moving to higher polymer concentrations. Considering that water vapor permeability should be preserved, but at the same time the coating should provide a satisfying barrier effect, a compromise needs to be found between these two factors. Taking into account this need, cs04 and cs1 were considered to be the best formulations since they represent a good balance of the two features. On the contrary, cs02 and cs2 have been excluded since they do not meet the requirements; cs02 does not provide a satisfying barrier effect, while cs2 presents the lowest water vapor permeability of the tested formulations.

Taking into account these results, CeO<sub>2</sub> NPs were included in the cs04 and in the cs1 formulations, which can offer a barrier effect while guaranteeing surface permeability. To maximize the performances of the composite, we determined 25 ppm of NPs to be the ideal compromise to achieve optimal protective action while minimizing the amount of nanomaterial used. In terms of protective action, the final concentration of 25 ppm was selected following the catalytic activity assessment. Indeed, the results from the investigation on the NPs' activity in solution showed that concentrations of tens of ppm of nanocatalyst are

sufficient to provide high activity. The so-prepared coating formulations (cs04-NPs and cs1-NPs) have then been tested to evaluate their protective efficiency.

#### Fresco mock-ups ageing and coating performance assessment.

The CeO<sub>2</sub> NPs-chitosan coatings were applied to fresco mock-ups previously painted with cinnabar, a red HgS pigment. Alongside natural red earths, cinnabar was among the most prized pigments used by Greek and Roman artists, valued for its vivid and striking red hue. However, unlike natural earths, cinnabar was typically reserved for the most prominent spaces within elite residences, underscoring its high prestige and symbolic significance.<sup>29,33,34</sup> After archaeological excavation, gradual darkening of frescoes painted with cinnabar has been evidenced as a consequence of exposure to light, high relative humidity and chlorine ions accumulated over time (Figure S9a and S9b).<sup>81,82</sup> Unfortunately, up to now no coating strategy has been designed to prevent this color variation and, therefore, urgent action is needed to effectively tackle this problem. Taking into account the complexity of the system and the need for innovative approaches, we tested the ability of our protective coating to respond to the challenges posed by this system. To simulate the environment in which cinnabar degrades, the mock-ups coated with the protective nanocomposite formulation were exposed to a multifactorial deterioration pathway, as described by Neiman *et al.*<sup>83</sup> The complex degradation protocol mimics the typical deteriorating environment surrounding cinnabar-painted frescoes and involves the simultaneous exposure to UV radiation, high relative humidity and chlorine-based salts.

The degradation mechanisms leading to the color change remain debated (Figure S10), but three main hypotheses have been suggested: (1) the formation of photosensitive chlorine-based species, (2) the establishment of photoinduced redox processes, and (3) the phase transition between cinnabar (a-HgS) and metacinnabar (b-HgS).<sup>31,84–87</sup> In the last decade, the simultaneous occurrence of these processes has also been proposed. Radepon *et al.* suggest that both metallic mercury and chlorine-based species such as cordeiorite (a-Hg<sub>3</sub>S<sub>2</sub>Cl<sub>2</sub>) and calomel (Hg<sub>2</sub>Cl<sub>2</sub>) can be formed as a consequence of the reaction between a-HgS and gaseous ClO.<sup>88</sup> The formation of Hg(0) is a consequence of the mentioned redox process through which the sulphide ion can be converted into S(0) or even sulphate, at the same time as the mercury is reduced. The process is still chlorine-dependent since this species acts as a catalyst in the redox mechanism. As determined in two works that tackled this issue in the last 5 years,<sup>89,90</sup> the experimental proof of this mechanism is extremely challenging due to instrumental limitations. Indeed, the high vacuum required during XPS characterization can potentially cause the evaporation of Hg(0), making the presence of sulphate the only indication of a redox reaction happening.<sup>89</sup> At the same time, the distinction between cinnabar and metacinnabar is challenging as they share the same elemental composition, making them undistinguishable in elemental characterizations. Moreover, they have similar peaks in Raman spectra and the

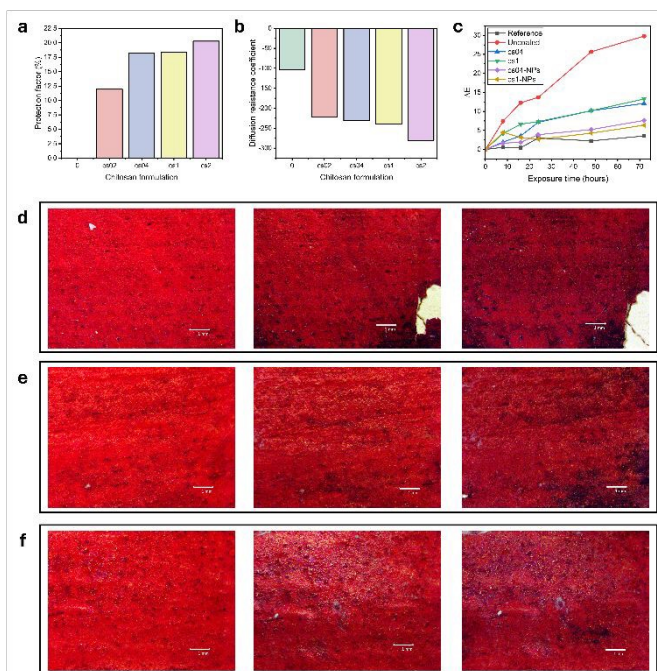


Figure 5. **a**, Protection factor of the four tested chitosan formulations after application on fresco mock-ups. **b**, Water vapor permeability of the four tested chitosan formulations after application on fresco mock-ups, reported as a measure of the water vapor resistance coefficient. **c**, Color variation of cinnabar fresco mock-ups coated with the cs04-NPs and cs1-NPs formulations after different ageing times. **d**, **e**, **f**, Microscope images of the cinnabar fresco mock-ups before ageing (left), after 24 hours of ageing (center), and after 72 hours of ageing (right); the uncoated mock-up (**d**), the one coated with cs04-NPs (**e**), and the one coated with cs1-NPs (**f**) are reported.





distinction generally requires techniques with high spatial resolution.<sup>90</sup> The current instrumental limitations are probably at the root of the debate, since clear identification of different species is fundamental to distinguish between several degradation pathways. In order to ascertain the mechanism involved in the present case study, we degraded an uncoated cinnabar-painted mock-up, and we performed both micro-Raman and XPS analyses. The results confirmed the experimental limitations previously reported in the literature (Figure S11a and S11b, and Figure S12a-d).

Considering the different mechanisms that have been proposed for the blackening of cinnabar, the protective strategy should provide a UV-shielding action, while at the same time blocking the redox mechanisms that can be catalyzed by the presence of chlorine-based species. CeO<sub>2</sub> NPs can act on both fronts thanks to their antioxidant activity and UV-shielding characteristics, which are also enhanced by the presence of a chitosan matrix. After the application of the two formulations to mock-ups and their simultaneous exposure to UV radiation and NaCl solution, we could confirm that the coating is able to inhibit the degradation of cinnabar and its consequent blackening. By monitoring the chromatic variation of the samples, it is clear that the color variation of the coated mock-ups is inferior compared to the uncoated sample (Figure 5c and Table S4). cs1-NPs achieve higher performances, as the only significant color variation happens within the first 8 hours of exposure. Differently, the uncoated sample shows great color variation at all steps of the degradation process and, after 72 hours, it presents the highest value of  $\Delta E$ . These observations confirm the positive effect of the NPs against the degradation caused by these environmental conditions. The microscope images confirm these results, determining that the blackening of the coated samples is slowed down or even completely prevented thanks to the presence of the coating (Figure 5d-f). Pictures of complete mock-ups (Table S5) further demonstrate the protection achieved thanks to the coating. Indeed, as clearly visible, black spots are already present on the uncoated sample after 8 hours of ageing. Contrarily, the black spots are formed in a small amount for the mock-up coated with cs04-NPs after 16 hours of ageing, whilst in the sample coated with cs1-NPs they cannot be observed at all even up to 48 hours of ageing. The improved performance of cs1-NPs compared to cs04-NPs could be linked to the different penetration of the coating in the porous substrate and, hence, to the different amount of the NPs present at the surface. Indeed, since cs04-NPs is less viscous, it is likely to partially enter the porous structure of fresco mock-ups, reducing the amount of functional nanomaterial present at the surface and able to protect the pigment. These considerations show that the rheological and filming properties of the cs04 formulation are not suitable for application on highly porous materials. The same conclusions can be drawn from the comparison between the protective ability of CeO<sub>2</sub> NPs-based coatings and the one of cs04 and cs1, without the addition of the NPs. While the addition of NPs in cs1 leads to clear improvements in its protective ability, the role of the NPs in cs04 appears to be marginal (Table S5). Both cs04 and cs04-NPs start to fail after about 16 hours of ageing, suggesting that the

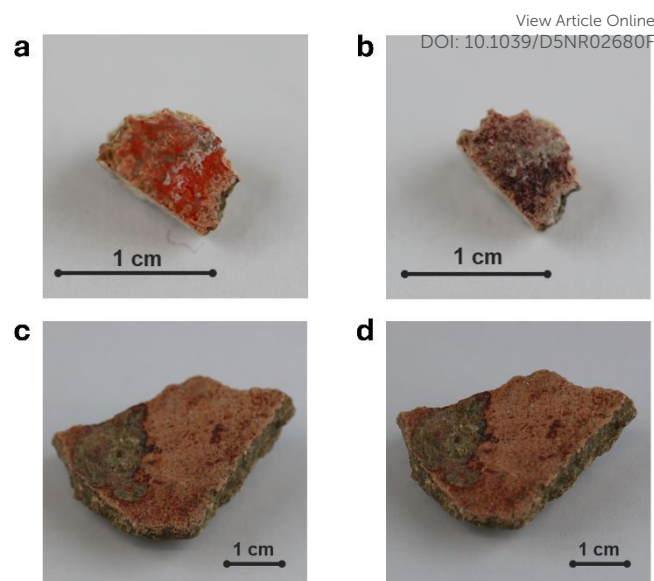


Figure 6. **a**, Uncoated fresco fragment before the degradation protocol. **b**, Uncoated fresco fragment after simultaneous exposure to UV-light, chlorine-based salts, and high relative humidity. **c**, Fresco fragment coated with cs1-NPs before the degradation protocol. **d**, Fresco fragment coated with cs1-NPs after simultaneous exposure to UV-light, chlorine-based salts, and high relative humidity.

NPs are not exerting any protective action. The effect can be attributed to the unsuitability of the cs04 polymeric matrix at confining the NPs at the surface.

Considering the successful results achieved with cs1-NPs formulation, we extended the investigation to a real case study by testing the effectiveness of the coating on precious frescoes fragments from the archaeological site of Aquileia (Italy). Cinnabar has been identified in both the tested fragments, as confirmed from the Raman spectrum reported in Figure S13. In Figure 6, the comparison between the coated and the uncoated sample exposed to the same ageing protocol confirms the protective action of the coating. While a distinct darkening can be observed on the uncoated surface, no changes have been detected on the coated fragment. This opens the application of the coating to the crucial task of frescoes' protection in important archaeological sites, where outdoor conditions constantly threaten their conservation.

The effectiveness of the cs1-NPs coating in protecting the substrate from darkening determines that the synergy between the NPs and the biopolymeric matrix has been successfully achieved. Furthermore, the effective protection achieved by using only 25 ppm of nanocatalyst shows that we have overcome important hindering effects of the catalytic sites that the organic biopolymeric matrix might have provoked. With this result, we show that we have effectively overcome the limitations linked to the introduction of CeO<sub>2</sub> NPs in organic formulations that were reported in previous works.

## Conclusions

In this work, we successfully developed a functional coating able to protect complex substrates from deterioration pathways



induced by exposure to a multifaceted environment. In particular, we designed a microwave-assisted synthesis method to produce ultra-small CeO<sub>2</sub> NPs with enhanced surface-to-volume ratio and high colloidal stability. Our protocol yields citrate-coated, non-stoichiometric NPs, with a remarkable content of Ce(III), endowing the nanocatalysts with exceptional antioxidant properties and versatility. We have established a well-defined structure-function relationship by demonstrating the Ce(III)/Ce(IV) redox cycling of the NPs using *in situ* Environmental XPS and linking the results to the catalytic performances. This approach represents a significant advancement, as we have achieved precise and reproducible control over surface chemistry and redox properties.

Furthermore, we leveraged the synergistic interaction between the NPs and chitosan to develop a protective composite coating that offers superior barrier properties alongside prolonged antioxidant activity. We demonstrated that the NPs-based catalytic shield successfully prevents the complex degradation processes of cinnabar induced by the combined exposure to UV light, chlorine-based salts, and high relative humidity. In summary, this strategy delivers efficient and multifactorial protection, highlighting the potential of ultra-small CeO<sub>2</sub> NPs-based composites as high-performance coatings for a wide range of technological applications.

## Experimental

### Synthesis of CeO<sub>2</sub> NPs.

Cerium(III) nitrate hexahydrate [Ce(NO<sub>3</sub>)<sub>3</sub>·6H<sub>2</sub>O], sodium citrate tribasic dihydrate, ammonium hydroxide solution (NH<sub>4</sub>OH, 28.0 – 30.0%), and tetramethylammonium hydroxide solution (TMAOH, 10%) were purchased from Sigma-Aldrich, Merck. All chemicals were used as received without further purification and ultrapure water (Millipore system) was used for all syntheses. The microwave-assisted synthesis was designed starting from a previously published protocol.<sup>57</sup> Briefly, Ce(NO<sub>3</sub>)<sub>3</sub>·6H<sub>2</sub>O (0.1 mmol) and sodium citrate (0.2 mmol) were mixed into 5 mL of ultrapure water and stirred until complete solubilization. NH<sub>4</sub>OH (or TMAOH) was added to reach a pH of 10. The solution was then stirred overnight at room temperature. The hydrothermal protocol was implemented in a Milestone Ethos UP microwave (Milestone srl, Bergamo, Italy), utilizing a multi-vessel system in which the temperature was increased to 100°C over 15 minutes and maintained for 30 minutes. Subsequently, the vessels were allowed to cool down to 50°C over 20 minutes before being removed. Following 2 hours of cooling to room temperature, the final products were purified by means of Amicon® Ultra membrane filters (3K).

### Chitosan formulation optimization.

Chitosan (cs, medium molecular weight), lactic acid (≥85%), azelaic acid (98%), sodium hydroxide (NaOH, ≥98%), and glycerol (HOCH<sub>2</sub>CH(OH)CH<sub>2</sub>OH, 99.0 – 101.0%) were purchased from Sigma-Aldrich, Merck. All chemicals were used as received without further purification and ultrapure water (Millipore

system) was used for all preparations. Starting from a published work,<sup>56</sup> a chitosan formulation was optimized by increasing the concentration of the biopolymer to achieve better filming properties and barrier effect. To summarize, azelaic acid (28wt% on a chitosan basis) was added to 50 mL of ultrapure water and the mixture was stirred until complete dissolution. Chitosan was added in different amounts to reach a concentration of 0.2 % (w/V), 0.4 % (w/V), 1.0 % (w/V), and 2.0 % (w/V) respectively for each formulation. The mixture was then heated to 95 °C while stirring at 600 rpm and lactic acid (60wt% on a chitosan basis) was added once the temperature was reached. The mixture was allowed to cool down and then glycerol was added. In order to neutralize the formulation, a 0.3 M solution of NaOH was added until the pH reached 8.

### Frescoes mock-ups preparation and coating.

In order to test our coatings on samples replicating as much as possible the complexity of frescoes, we produced fresco mock-ups starting from historical Vitruvius recipes, while also simplifying the preparation process to facilitate high-throughput screening of the coatings. Natural cinnabar (#10620) and marble dust (powder, < 200 μm) were purchased from Kremer Pigmente, while lime putty and coarse quartzite (0.1 – 0.3 mm) were acquired from CTS Conservation. Coarse-grained river sand (0 – 1 mm) from AXTON was purchased from Leroy Merlin.

The simplified samples were obtained by solely reproducing the outer layers of frescoes, *i.e.* the *intonachino* covered by the pigment layer. In particular, we employed laboratory glass slides as a support for the mortar layer, and we wrapped a gauze strip (10 cm x 5 cm) around it to guarantee good gripping. We prepared *intonachino* by mixing marble dust and lime putty in a 1:1 ratio and by adding water when necessary. We applied the *intonachino* on the support and we painted it with cinnabar dispersed in ultrapure water before it dried, following the traditional fresco technique. The mock-ups were allowed to carbonate for 3 months.

Complete fresco mock-ups were also prepared to test the protection factor and the water vapor permeability of the coatings. The procedure for the outer layers remains the same as the one described for the simplified mock-ups. However, beneath the *intonachino* layer, the *arriccio* layer is first prepared. *Arriccio* is obtained by mixing lime putty, coarse quartzite and coarse-grained river sand in a 1:1:1 ratio and adding enough water (*q.s.*) to achieve adequate workability of the mortar. The mock-ups were allowed to carbonate for 6 months.

The two types of mock-ups are schematically represented in Figure S14. After carbonation they were coated with the chitosan formulations or with the composite CeO<sub>2</sub> NPs-based chitosan formulations by brush-painting (0.125 mL cm<sup>-2</sup>).

### Characterization of CeO<sub>2</sub> NPs.

X-ray diffraction (XRD) patterns were acquired with a Malvern-PANalytical third generation Empyrean X-ray diffractometer, operating at 60 kV and 40 mA and equipped with a 2.5 kW Mo



K $\alpha$  X-ray tube, GaliPIX3D solid-state pixel detector. The diffraction pattern was collected in transmission geometry, from 8° to 80° with a step size of 0.043° and scan speed = 1.2° min<sup>-1</sup>, using a Mo focusing mirror, a reflection-transmission spinner sample stage (rotation speed = 1 rps) and 5  $\mu$ m Mylar foil as sample substrate. Size and strain analysis was performed with HighScore Plus 5.3 software and the whole-powder-pattern decomposition (WPPD) technique based on the Pawley algorithm. The instrumental broadening was removed using a diffraction pattern collected from the NIST LaB6 (SRM 660) standard. The characterization was performed in powder form: 1 mL of CeO<sub>2</sub> NPs dispersion was freeze-dried overnight to remove the solvent and obtain a solid sample.

Bright-field transmission electron microscopy (BF-TEM) analyses were performed by means of a JEOL JEM-1011 microscope with a thermionic source (W filament), operated at 100 kV. TEM images were analyzed with the software ImageJ to determine the average diameter of the NPs; in each image the diameter of 100 NPs was measured to obtain an average value. A small volume of each sample diluted 1:1 with methanol was drop-casted onto carbon/Cu grids (300 mesh). To investigate the crystallinity at the nanoscale, high-resolution TEM (HR-TEM) was performed with image-Cs-corrected JEOL JEM-2200FS TEM, equipped with in-column image filter ( $\Omega$ -type), operated at 200 kV. The HR-TEM images presented here have been acquired using a direct-electron-detection camera (K2 Summit, Gatan), so as to reduce beam damage (e.g., carbon contamination build-up). A small volume of each sample was drop-casted onto ultrathin carbon/holey carbon/Cu grids. Then, small-angle X-ray scattering (SAXS) analysis was performed using a Malvern PANalytical third generation Empyrean multipurpose platform in transmission geometry with Cu K $\alpha$  radiation ( $\lambda$  = 1.54 Å; 40 kV, 45 mA). 1D-SAXS measurements were carried out in a vacuum path chamber (Scatter X78) using a beam with line collimation and a GaliPIX3D detector. Quartz capillaries (Hilgenberg, DE) with a 1 mm diameter (100  $\mu$ L volume) were used. Background measurement of ultrapure pure water was performed in the same capillary used for the NPs dispersions. Scans were performed in the  $q$  region 0.1 – 3.5 nm<sup>-1</sup> with step size 0.014°, with an exposure time of 30 min. The data analysis was performed using the EasySAXS software (Malvern-PANalytical). The software performs primary data handling steps, including absorption correction, background-subtraction, and conversion of the scattering angle  $2\theta$  to the scattering vector  $q$ . Determination of NPs distribution was done by an indirect integral transform technique that relates experimental SAXS data to the volume distribution function  $Dv(R)$  using a regularization procedure.

#### Redox cycling of CeO<sub>2</sub> NPs.

Environmental X-ray photoelectron spectroscopy (XPS) was used to determine the relative Ce(III)/Ce(IV) ratio on the surface of the NPs and to study how this ratio evolves when the NPs are subjected to different oxidizing and reducing agents (i.e., O<sub>2</sub>, H<sub>2</sub>O<sub>2</sub>, UV radiation, and high temperature). For this analysis, we used the EnviroESCA system (SPECs Electron Spectroscopy for

Chemical Analysis Under Environmental Conditions, GmbH, Germany) with a monochromated Al K $\alpha$  X-ray source (1486.6 eV), present at Charles University, Prague. The analyzer (SPECs PHOIBOS 150) operates under ultra-high vacuum conditions (10<sup>-9</sup> mbar), and signal detection was conducted in FAT (Fixed Analyzer Transmission) mode.

During the XPS measurements, the core-level spectra of Ce 3d, Na 1s, C 1s, O 1s, and the valence band were recorded with a pass energy of 20 eV, a step size of 0.1 eV, and a dwell time of 0.3 seconds. Both the fresh NPs and the ones exposed to natural light for 3 months under conventional laboratory conditions were drop-casted on silicon wafer substrates and were analyzed under a 1 mbar Ar atmosphere with a 25 mL min<sup>-1</sup> flow during the measurement. The same measurement was repeated for the fresh NPs in an O<sub>2</sub> atmosphere and then the NPs were treated with a 1 M solution of H<sub>2</sub>O<sub>2</sub> (10:1 ratio) and analyzed in the Ar atmosphere. Lastly, the NPs were drop-cast onto the CHU01 (Cooling Heating Unit), which was connected through the EnviroESCA interface. The temperature was monitored by a thermocouple on the heating unit, which was heated up to 300°C. The spot size was 200  $\mu$ m.

Through an *ad hoc* engineered cell system,<sup>91</sup> the oxidations states of the NPs were also investigated while in an ultrapure water solution, in the presence or absence of H<sub>2</sub>O<sub>2</sub>. The binding energy scale was referenced to the Ce<sup>4+</sup> 3d<sub>3/2</sub> U<sup>III</sup> peak at 916.7 eV and spectra elaboration was then carried out by CasaXPS software (2.3.25 version). An U2 Tougaard background was applied across the binding energy range of the peaks of interest.

#### Oxygen-related catalytic activity of CeO<sub>2</sub> NPs.

Hydrogen peroxide (H<sub>2</sub>O<sub>2</sub>, 30%) was purchased from Sigma-Aldrich, Merck. 3,3',5,5'-Tetramethylbenzidine (TMB), was obtained from Kementec, Denmark. All chemicals were used as received without further purification and ultrapure water (Millipore system) was used for all solutions preparation. TMB was employed as a chromogenic substrate to investigate the peroxidase- and oxidase-like activity of CeO<sub>2</sub> NPs. Peroxidase-like activity was determined by using H<sub>2</sub>O<sub>2</sub> as a substrate, in a system containing a mixture of TMB and H<sub>2</sub>O<sub>2</sub> (1 M) in a 1:1.6 ratio. Oxidase-like activity was tested by using molecular oxygen dissolved in water from the atmosphere as a substrate.

In both cases, the characteristic peak of the oxidized form of TMB at 652 nm was monitored by collecting the UV-visible spectra with a double beam Agilent Cary 100 Series UV-Vis spectrophotometer (Agilent Technologies, Santa Clara, CA, USA) at room temperature. The spectra were collected in the 800 – 200 nm range through the CaryWinUV Scan software (4.20 version). They were then elaborated by means of OriginPro 2022 software (OriginLab Corporation, Northampton, MA, USA). UV-visible spectra are reported in the range 500 – 800 nm, which is the region where the mono-oxidized form of TMB absorbs. This region is otherwise free of signals, as can be observed from the UV-visible spectra of the NPs reported in Figure S4a and S4b.

The effect of CeO<sub>2</sub> NPs concentration and the kinetic trend of this interaction were studied; the activity was tested in the





concentration range 0.1 – 25 ppm, including the control test of the chromogenic substrate in the absence of the nanocatalyst (0 ppm). The spectra were collected 5, 10 and 15 min after the addition of TMB.

#### Biocompatibility assays of CeO<sub>2</sub> NPs.

The stability of the NPs was compared with two commercial ones (Cerium(IV) oxide 20% in H<sub>2</sub>O, < 5.0 nm, Alfa Aesar; Cerium(IV) oxide nanopowder, < 25 nm, Sigma-Aldrich). In order to study the interaction between proteins and CeO<sub>2</sub> NPs, they were incubated for 2 h at room temperature and in mild agitation in an aqueous solution containing 50% heat-inactivated fetal bovine serum (FBS, Gibco). Subsequently the NPs were rinsed to remove any unbounded serum proteins.

A stability assay in cell culture medium was performed on 100 ppm dispersions of the NPs. We used Dulbecco's Modified Eagle Medium (DMEM, Gibco) supplemented with 20% of heat-inactivated fetal bovine serum (FBS, Gibco), 1% L-glutamine (stock 200 mM, Gibco), and 1% penicillin-streptomycin (100 IU mL<sup>-1</sup> of penicillin and 100 µg mL<sup>-1</sup> of streptomycin, Gibco). In these analyses, the hydrodynamic diameters ( $d_h$ ) were analyzed over 1 h with single acquisitions every 12 min, and over 72 h with acquisitions every 24 h. For the determination of the average  $d_h$ , dynamic light scattering measurements have been performed using a Malvern Zetasizer Nano ZS90 instrument. The values were assessed using a 100 ppm dispersion in polystyrene cuvettes.

The cytotoxicity effect of the CeO<sub>2</sub> NPs we synthesized was assessed *in vitro* through the PicoGreen assay (QuantiT PicoGreen dsDNA Assay Kit, Invitrogen) that allows an indirect evaluation of cell proliferation through dsDNA concentration assessment. Cells were seeded in 96-well plates (Corning) at 10,000 cells cm<sup>-2</sup> and incubated overnight, thereafter, cells were treated for 24 and 72 h with increasing concentrations of NPs (0.0, 6.25, 12.50, 25.00, 50.00, and 100.0 ppm). At the end of the incubation, cultures were washed with Dulbecco's phosphate-buffered saline (DPBS, Gibco) and the medium was replaced with 100 µL of ultrapure water. Four freeze/thaw cycles (from -80 to 37 °C) were performed to allow cell lysis and dsDNA release. The dsDNA quantification was carried out in Corning Costar 96-well black polystyrene plates following the manufacturer's instructions. Fluorescence levels were detected with a Victor X3Multilabel Plate Reader ( $\lambda_{ex}$  360,  $\lambda_{em}$  460 nm) and correlated to the dsDNA content and thus to the cell number.

Further information on the cytotoxicity effect of the NPs was achieved by performing the LIVE/DEAD cell viability assay (ThermoFisher), according to the manufacturer's instructions. Cells were seeded in µ-Plate 96-Well Black (Ibidi) at 10,000 cells cm<sup>-2</sup> and incubated overnight. Thereafter, cells were treated for 72 h with increasing concentrations of NPs (0.0, 6.25, 12.50, 25.00, 50.00, and 100.0 ppm). After the treatment cultures were rinsed with DPBS and incubated for 20 min with fresh medium containing 5 µg mL<sup>-1</sup> Hoechst, 4 µM ethidium homodimer-1 (Thermo Fisher), and 2 µM calcein-AM (Thermo Fisher). Imaging was performed with a fluorescence microscope

(Eclipse Ti, Nikon) equipped with a 10× objective. The acquired images were subjected to analysis using ImageJ, where the relative quantities of dead cells (ethidium homodimer-1-positive cells) and viable cells (calcein-positive cells) were counted within each specific condition.

Inductively coupled plasma mass spectrometry (ICP-MS) was used to evaluate the cellular uptake of the NPs. Cells were seeded at 10,000 cells cm<sup>-2</sup> density and incubated overnight; thereafter, half of the samples were treated for 72 h with a 100 ppm NPs concentration. Then cells were detached and counted to determine their number and subsequently resuspended in DPBS for the following ICP-MS analysis.

#### Characterization and performance evaluation of the chitosan formulation.

We compared the morphology of the formulations through scanning electron microscopy (SEM) analysis, by means of a JEOL JSM-6490LA microscope with a thermionic source (W filament).

The viscosity of the formulations was determined to choose the best application method. The rheology analyses were performed by using a Modular Compact Rheometer (MCR 102) from Anton Paar GmbH, with a No. 3912 coaxial cylinder measuring system. 5 mL of each formulation were poured in the cylindrical cup (radius of 14.452 mm), using a measuring bob with a radius of 13.331 mm, a Ratio of Radii of 1.084, and a Gap Length of 39.998 mm. Each measurement was acquired with a cone angle of 120° and a measuring gap of 1.121 mm. The RheoCompass software was used to collect data, which were then processed with the OriginPro 2022 software (OriginLab Corporation, Northampton, MA, USA).

After applying the formulation to the mock-ups, the coating was studied in terms of morphology, color variation, surface water contact angle, protecting ability, and water vapor permeability. The morphological analyses were performed by collecting images of the mock-ups before and after the application of the coating through a NYKON stereomicroscope model SMZ 745T (European Headquarters Nikon Europe BV, Tripolis 100, Burgerweeshuispad 101, 1076 ER Amsterdam, Netherlands). Additionally, the color variation produced by the application of the coating was monitored by means of a Konica Minolta CM 700d spectrophotometer, with an 8-degree viewing angle geometry, a diffusion light Xenon lamp, and a high-resolution monolithic polychromator. A circular area with a diameter of 8 mm was tested for each measure, and the results were obtained as the average of three different measures carried out on different mock-ups treated with the same coating formulation. Measurements were performed in the CIELAB1976 space and elaboration was carried out by means of Spectra Magic NX software. The color variation is defined in terms of  $\Delta E$ , which is calculated as follows.<sup>92</sup>

$$\Delta E = \sqrt{\Delta L^2 + \Delta a^2 + \Delta b^2}$$

where  $\Delta L$ ,  $\Delta a$ , and  $\Delta b$  are the differences between the values obtained before and after the application of the coating on each sample. The parameters represent luminosity, red-green, and blue-yellow, respectively.



The surface contact angle was measured by means of a FTA 1000 Analyzer System (First Ten Angstroms Inc., Newark, CA, USA), by dropping a 10  $\mu\text{L}$  drop of water on the surface and instantaneously acquiring an image of said drop. The measurements were acquired on three different points of the surface of each mock-up. The contact angle was then determined by analyzing each image with the software ImageJ and averaging the obtained contact angles for each formulation.

The protective ability of the coating and the water vapor permeability were determined by following the norms UNI 10921:2001<sup>93</sup> and UNI 15803:2010<sup>94</sup> respectively.

#### **Fresco mock-ups ageing and coating performance assessment.**

CeO<sub>2</sub> NPs were added to the cs04 and cs1 formulations to reach a final concentration of 25 ppm. The addition was performed at room temperature while stirring at 800 rpm during the preparation of the formulation. The coating formulations were applied to the surface of simplified mock-ups as previously described (brush-painting; 0.125 mL cm<sup>-2</sup>). In order to test the efficacy of the CeO<sub>2</sub> NPs-based coating, the coated mock-ups and an uncoated sample underwent an accelerated ageing protocol, as described in a previous study.<sup>83</sup> First, they were placed in closed plastic petri dishes containing a 0.1 M NaCl solution at 27.0 °C, making sure that only the bottom part of the sample came into contact with the solution itself. This allows to reproduce the interaction with chlorine-based salts through capillary absorption from the bottom of the structure. The exposure to the NaCl solution was operated in the dark for 12 hours. Then, while the samples were still wet, they were placed in a Q-Sun Xe-1S climatic chamber (Q-LAB Corporation, Westlake, OH 44145-1419 SUA) and they were exposed to 8 hours cycles of UV light (65 W m<sup>-2</sup>) at 50 °C, up to 72 hours of total exposure. Exposure to UV light in wet conditions simulates a highly humid environment.

Two archaeological fresco fragments were also exposed to this same degradation protocol, limited to 72 hours of UV-exposure. One of these samples was preemptively coated with formulation cs1-NPs, while the other was considered as a reference of normal degradation. Visible aesthetic variations were monitored by acquiring photographs of the fragments before and after the degradation.

Between each repetition, the samples were tested in terms of morphologic and color variation, as described in the study of the chitosan coating in the previous section. Each acquisition was performed on two distinct points of the surface of each mock-up to account for heterogeneity and the colorimetric measurements were performed as an average of three measurements on each spot. After the completion of the tests, Raman spectra were acquired in different spots of the uncoated sample to determine the chemical composition of the degraded and non-degraded portions. A Raman Microscope DXRTM3 with a 532 nm laser source was used to acquire the spectra. The conditions of each measurement were kept constant to better compare the results from different areas. Laser power level was set to 1.0 mW with a grating of 900 lines mm<sup>-1</sup>, the 10x

microscope objective was used, and the 25  $\mu\text{m}$  pinhole aperture was set. Each measurement was collected after 2 exposures of 60 seconds, with a resolution of 1.9285 Raman shift (cm<sup>-1</sup>). After the surface characterization, a portion of the pictorial layer was removed from the uncoated samples, and the powder was characterized through XPS. This last characterization was performed by means of a Kratos Axis UltraDLD spectrometer (Kratos Analytical Ltd.) with a monochromated Al K $\alpha$  X-ray source (h $\nu$  = 1486.6 eV) operating at 20 mA and 15 kV. Each specimen, in powder form, was prepared by pressing about 500 mg of powder onto a conductive indium substrate, to obtain a film as much flat as possible. The wide scans were collected over an analysis area of 300  $\times$  700  $\mu\text{m}^2$  at a photoelectron pass energy of 160 eV and energy step of 1 eV, while high-resolution spectra of Hg 4f and S 2p were collected at a photoelectron pass energy of 20 eV and an energy step of 0.1 eV. A take-off angle of 0° with respect to sample normal direction was used for all analyses. The differential electrical charging effects observed on all samples were neutralized. The spectra have been referenced to the adventitious carbon 1s peak at 284.8 eV. The spectra were analyzed with the CasaXPS software (Casa Software Ltd., version 2.3.25),<sup>95</sup> and the residual background was eliminated by the Shirley method across the binding energy range of the peaks of interest.

#### **Author contributions**

Conceptualization: EG, GC, FM, AT, MM

Methodology: EG, SM, SD, RB, MGR, FM, MM

Investigation: EG, SM, SD, RB, AC, MB, MM

Visualization: EG, SM, SD, RB, AC, MB, MM

Supervision: GC, FM, AT, MM

Writing—original draft: EG, FM, AT, MM

Writing—review & editing: EG, SM, SD, RB, AC, RL, FM, AT, MM

#### **Conflicts of interest**

There are no conflicts to declare.

#### **Data availability**

All data collected within this research is reported in the main text of the article and in its Supplementary Information. In the Supplementary Information file, additional data on the characterization of the nanoparticles and of the coating and additional information on the case study described are available.

#### **Acknowledgements**

The authors acknowledge the CERIC-ERIC Consortium for the access to experimental facilities and financial support. We are grateful to Federico Catalano, Tania Fantinel, and Filippo Drago for performing SEM and ICP-MS analyses. We also thank Francesco De Boni who performed XPS characterization and Tomáš Hrbek for his help with Environmental XPS measurements.



The fresco fragments shown in this article are identified with the Italian National ID 586026 and have been gently provided by the Museo archeologico nazionale di Aquileia – Italia. Images in Figure 6 are used on authorisation of the Ministero della cultura, Museo Storico e Parco del Castello di Miramare - Direzione regionale Musei nazionali Friuli Venezia Giulia. The use of these images is regulated by current legislation (art. 108, co. 3 del D. Lgs 42/2004 s.m.i. - DM 161/23 – DM 108/24). Any reproduction, duplication or manipulation is strictly prohibited.

## References

- G. Xiao, H. Li, Y. Zhao, H. Wei, J. Li and H. Su, *ACS Appl. Nano Mater.*, 2022, **5**, 14147–14170.
- K. Reed, A. Cormack, A. Kulkarni, M. Mayton, D. Sayle, F. Klaessig and B. Stadler, *Environ. Sci.: Nano*, 2014, **1**, 390–405.
- F. Caputo, M. D. Nicola, A. Sienkiewicz, A. Giovanetti, I. Bejarano, S. Licocchia, E. Traversa and L. Ghibelli, *Nanoscale*, 2015, **7**, 15643–15656.
- Y. Li, X. Hou, C. Yang, Y. Pang, X. Li, G. Jiang and Y. Liu, *Sci Rep*, 2019, **9**, 2595.
- R. Huang, X. Du, H. Wang, X. Cheng and Z. Du, *Journal of Applied Polymer Science*, 2022, **139**, 51927.
- R. Álvarez-Asencio, R. W. Corkery and A. Ahniyaz, *RSC Advances*, 2020, **10**, 14818–14825.
- S. Yasmeen, M. R. Khan, K. Park, Y. Cho, J. W. Choi, H.-S. Moon and H.-B.-R. Lee, *Ceramics International*, 2020, **46**, 12209–12215.
- S. V. Harb, A. Trentin, T. A. C. de Souza, M. Magnani, S. H. Pulcinelli, C. V. Santilli and P. Hammer, *Chemical Engineering Journal*, 2020, **383**, 123219.
- K. An, Y. Sui, Y. Qing, C. Yang, C. Long, L. Wang and C. Liu, *Colloids and Surfaces A: Physicochemical and Engineering Aspects*, 2021, **625**, 126904.
- B. Fotovvat, M. Behzadnasab, S. M. Mirabedini and H. E. Mohammadloo, *Colloids and Surfaces A: Physicochemical and Engineering Aspects*, 2022, **648**, 129157.
- A. Joseph, K. P. John Mathew and S. Vandana, *ACS Appl. Nano Mater.*, 2021, **4**, 834–849.
- I. Martín-Fabiani, M. L. Koh, F. Dalmás, K. L. Elidottir, S. J. Hinder, I. Jurewicz, M. Lansalot, E. Bourgeat-Lami and J. L. Keddie, *ACS Appl. Nano Mater.*, 2018, **1**, 3956–3968.
- K. An, Y. Wang, Y. Sui, Y. Qing, W. Tong, X. Wang and C. Liu, *Journal of Rare Earths*, DOI:10.1016/j.jre.2024.03.017.
- L. G. Ecco, M. Fedel, A. Ahniyaz and F. Deflorian, *Progress in Organic Coatings*, 2014, **77**, 2031–2038.
- S. Fu, Z. Sun, P. Huang, Y. Li and N. Hu, *Nano Materials Science*, 2019, **1**, 2–30. DOI: 10.1039/D5NR02680F
- J. Janesch, I. Czabany, C. Hansmann, A. Mautner, T. Rosenau and W. Gindl-Altmutter, *Progress in Organic Coatings*, 2020, **138**, 105409.
- N. Karak, in *Nanomaterials and Polymer Nanocomposites*, ed. N. Karak, Elsevier, 2019, pp. 1–45.
- K. Zarschler, L. Rocks, N. Licciardello, L. Boselli, E. Polo, K. P. Garcia, L. De Cola, H. Stephan and K. A. Dawson, *Nanomedicine: Nanotechnology, Biology and Medicine*, 2016, **12**, 1663–1701.
- B. H. Kim, M. J. Hackett, J. Park and T. Hyeon, *Chem. Mater.*, 2014, **26**, 59–71.
- E. Spielman-Sun, E. Lombi, E. Donner, D. Howard, J. M. Unrine and G. V. Lowry, *Environ. Sci. Technol.*, 2017, **51**, 7361–7368.
- C. K. Kim, T. Kim, I.-Y. Choi, M. Soh, D. Kim, Y.-J. Kim, H. Jang, H.-S. Yang, J. Y. Kim, H.-K. Park, S. P. Park, S. Park, T. Yu, B.-W. Yoon, S.-H. Lee and T. Hyeon, *Angewandte Chemie International Edition*, 2012, **51**, 11039–11043.
- T. V. Plakhova, A. Y. Romanchuk, S. M. Butorin, A. D. Konyukhova, A. V. Egorov, A. A. Shiryaev, A. E. Baranchikov, P. V. Dorovatovskii, T. Huthwelker, E. Gerber, S. Bauters, M. M. Sozarukova, A. C. Scheinost, V. K. Ivanov, S. N. Kalmykov and K. O. Kvashnina, *Nanoscale*, 2019, **11**, 18142–18149.
- A. L. Popov, N. R. Popova, N. V. Tarakina, O. S. Ivanova, A. M. Ermakov, V. K. Ivanov and G. B. Sukhorukov, *ACS Biomater. Sci. Eng.*, 2018, **4**, 2453–2462.
- A. L. Popov, N. Popova, D. J. Gould, A. B. Shcherbakov, G. B. Sukhorukov and V. K. Ivanov, *ACS Appl. Mater. Interfaces*, 2018, **10**, 14367–14377.
- A. L. Popov, N. R. Popova, I. I. Selezneva, A. Y. Akkizov and V. K. Ivanov, *Materials Science and Engineering: C*, 2016, **68**, 406–413.
- R. Mehmood, N. Ariotti, J. L. Yang, P. Koshy and C. C. Sorrell, *ACS Biomater. Sci. Eng.*, 2018, **4**, 1064–1072.
- E. Grulke, K. Reed, M. Beck, X. Huang, A. Cormack and S. Seal, *Environ. Sci.: Nano*, 2014, **1**, 429–444.
- S. Seal, A. Jeyaranjan, C. J. Neal, U. Kumar, T. S. Sakthivel and D. C. Sayle, *Nanoscale*, 2020, **12**, 6879–6899.
- M. Maguregui, U. Knuutinen, K. Castro and J. M. Madariaga, *Journal of Raman Spectroscopy*, 2010, **41**, 1400–1409.
- M. Cotte, J. Susini, N. Metrich, A. Moscato, C. Gratzu, A. Bertagnini and M. Pagano, *Anal. Chem.*, 2006, **78**, 7484–7492.





- 31 M. Radepont, W. de Nolf, K. Janssens, G. V. der Snickt, Y. Coquinot, L. Klaassen and M. Cotte, *J. Anal. At. Spectrom.*, 2011, **26**, 959–968.
- 32 F. Da Pieve, C. Hogan, D. Lamoën, J. Verbeeck, F. Vanmeert, M. Radepont, M. Cotte, K. Janssens, X. Gonze and G. Van Tendeloo, *Phys. Rev. Lett.*, 2013, **111**, 208302.
- 33 M. Salvadori and C. Sbrolli, *Archaeol Anthropol Sci*, 2021, **13**, 187.
- 34 D. Jiménez-Desmond, J. S. Pozo-Antonio and A. Arizzi, *Journal of Cultural Heritage*, 2024, **66**, 166–186.
- 35 P. Fermo, G. Cappelletti, N. Cozzi, G. Padeletti, S. Kaciulis, M. Brucale and M. Merlini, *Appl. Phys. A*, 2014, **116**, 341–348.
- 36 J. Brus and P. Kotlík, *Studies in Conservation*, 1996, **41**, 109–119.
- 37 A. Tsakalof, P. Manoudis, I. Karapanagiotis, I. Chrysosoulakis and C. Panayiotou, *Journal of Cultural Heritage*, 2007, **8**, 69–72.
- 38 S. A. Ruffolo and M. F. La Russa, *Front. Mater.*, DOI:10.3389/fmats.2019.00147.
- 39 M. Zucchelli, G. Mazzon, L. Bertolacci, R. Carzino, E. Zendri and A. Athanassiou, *Progress in Organic Coatings*, 2021, **159**, 106434.
- 40 S. Andreotti, E. Franzoni, M. Degli Esposti and P. Fabbri, *Materials*, 2018, **11**, 165.
- 41 S. Mandal, P. Kumar, B. Satpathy, K. Das and S. Das, *Journal of Cultural Heritage*, 2024, **69**, 94–112.
- 42 D. Colangiuli, M. Lettieri, M. Masieri and A. Calia, *Science of The Total Environment*, 2019, **650**, 2919–2930.
- 43 P. M. Carmona-Quiroga, S. Martínez-Ramírez and H. A. Viles, *Applied Surface Science*, 2018, **433**, 312–320.
- 44 M. F. La Russa, N. Rovella, M. Alvarez de Buergo, C. M. Belfiore, A. Pezzino, G. M. Crisci and S. A. Ruffolo, *Progress in Organic Coatings*, 2016, **91**, 1–8.
- 45 P. Munafò, G. B. Goffredo and E. Quagliarini, *Construction and Building Materials*, 2015, **84**, 201–218.
- 46 L. O. Cintează, M. A. Tănase, L. O. Cintează and M. A. Tănase, in *Thin Films*, IntechOpen, 2020.
- 47 S. A. Ruffolo, M. F. La Russa, M. Malagodi, C. Oliviero Rossi, A. M. Palermo and G. M. Crisci, *Appl. Phys. A*, 2010, **100**, 829–834.
- 48 S. A. Ruffolo, M. F. La Russa, P. Aloise, C. M. Belfiore, A. Macchia, A. Pezzino and G. M. Crisci, *Appl. Phys. A*, 2014, **114**, 753–758.
- 49 J. Otero, V. Starinieri, A. E. Charola and G. Taglieri, *Construction and Building Materials*, 2020, **230**, 117112.
- 50 J. Otero, V. Starinieri and A. E. Charola, *Construction and Building Materials*, 2018, **181**, 394–407.
- 51 M. J. Mosquera, L. A. M. Carrascosa and N. Badreldin, *Pure and Applied Chemistry*, 2018, **90**, 551–561.
- 52 A. Chatzigrigoriou, P. N. Manoudis and I. Karapanagiotis, *Macromolecular Symposia*, 2013, **331–332**, 158–165.
- 53 L. de Ferri, P. P. Lottici, A. Lorenzi, A. Montenero and E. Salvioli-Mariani, *Journal of Cultural Heritage*, 2011, **12**, 356–363.
- 54 I. Franco-Castillo, L. Hierro, J. M. de la Fuente, A. Seral-Ascaso and S. G. Mitchell, *Chem*, 2021, **7**, 629–669.
- 55 M. R. Caruso, G. D'Agostino, S. Milioto, G. Cavallaro and G. Lazzara, *J Mater Sci*, 2023, **58**, 12954–12975.
- 56 R. Lamuraglia, A. Campostrini, E. Ghedini, A. De Lorenzi Pezzolo, A. Di Michele, G. Franceschin, F. Menegazzo, M. Signoretto and A. Traviglia, *Coatings*, 2023, **13**, 277.
- 57 A. Badia, A. Duarri, A. Salas, J. Rosell, J. Ramis, M. F. Gusta, E. Casals, M. A. Zapata, V. Puentes and J. García-Arumí, *ACS Nano*, 2023, **17**, 910–926.
- 58 M. Kurian and C. Kunjachan, *Int Nano Lett*, 2014, **4**, 73–80.
- 59 R. K. Hailstone, A. G. DiFrancesco, J. G. Leong, T. D. Allston and K. J. Reed, *J. Phys. Chem. C*, 2009, **113**, 15155–15159.
- 60 E. G. Heckert, A. S. Karakoti, S. Seal and W. T. Self, *Biomaterials*, 2008, **29**, 2705–2709.
- 61 W.-J. Jeon, H. Kim and S.-H. Byeon, *Colloids and Surfaces A: Physicochemical and Engineering Aspects*, 2022, **640**, 128416.
- 62 T. Skála, F. Šutara, K. C. Prince and V. Matolín, *Journal of Electron Spectroscopy and Related Phenomena*, 2009, **169**, 20–25.
- 63 E. Bêche, P. Charvin, D. Perarnau, S. Abanades and G. Flamant, *Surface and Interface Analysis*, 2008, **40**, 264–267.
- 64 A. Murali, Y.-P. Lan and H. Y. Sohn, *Nano-Structures & Nano-Objects*, 2019, **18**, 100257.
- 65 Y. Ma, W. Gao, Z. Zhang, S. Zhang, Z. Tian, Y. Liu, J. C. Ho and Y. Qu, *Surface Science Reports*, 2018, **73**, 1–36.
- 66 J. Henych, M. Šťastný, J. Ederer, Z. Němečková, A. Pogorzelska, J. Tolasz, M. Kormunda, P. Ryšánek, B. Bažanów, D. Stygar, K. Mazanec and P. Janoš, *Environmental Science: Nano*, 2022, **9**, 3485–3501.



- 67 R. Priyadarshi and J.-W. Rhim, *Innovative Food Science & Emerging Technologies*, 2020, **62**, 102346.
- 68 L. Qi, S. Pal, P. Dutta, M. Seehra and M. Pei, *Journal of Biomedical Materials Research Part A*, 2008, **87A**, 236–244.
- 69 G. Thandapani, S. P. P., S. P. n. and A. Sukumaran, *International Journal of Biological Macromolecules*, 2017, **104**, 1794–1806.
- 70 Chitosan implants in the rat spinal cord: Biocompatibility and biodegradation - Kim - 2011 - Journal of Biomedical Materials Research Part A - Wiley Online Library, [https://onlinelibrary.wiley.com/doi/full/10.1002/jbm.a.33070?casa\\_token=rplEWb5TiQAAAAA%3AK\\_YzXK64dy-kDMRZtgwZSw0XbVv3wJMtKBnnN8k\\_ihaFK-h1Q5OdTgJRMub-snQ9iQ9Dyi8dw7E5](https://onlinelibrary.wiley.com/doi/full/10.1002/jbm.a.33070?casa_token=rplEWb5TiQAAAAA%3AK_YzXK64dy-kDMRZtgwZSw0XbVv3wJMtKBnnN8k_ihaFK-h1Q5OdTgJRMub-snQ9iQ9Dyi8dw7E5), (accessed September 1, 2025).
- 71 K. A. Dawson and Y. Yan, *Nat. Nanotechnol.*, 2021, **16**, 229–242.
- 72 G. G. Genchi, A. Degl'Innocenti, C. Martinelli, M. Battaglini, D. De Pasquale, M. Prato, S. Marras, G. Pugliese, F. Drago, A. Mariani, M. Balsamo, V. Zolesi and G. Ciofani, *ACS Appl. Mater. Interfaces*, 2021, **13**, 40200–40213.
- 73 G. G. Genchi, V. Mollo, M. Battaglini, M. Belenli Gümüş, A. Marino, M. Prato, S. Marras, F. Drago, G. Pugliese, F. Santoro and G. Ciofani, *ACS Appl. Nano Mater.*, 2023, **6**, 10853–10862.
- 74 M. Eppe, V. M. Rotello and K. Dawson, *Acc. Chem. Res.*, 2023, **56**, 3369–3378.
- 75 S. D. Purohit, R. Priyadarshi, R. Bhaskar and S. S. Han, *Food Hydrocolloids*, 2023, **143**, 108910.
- 76 P. K. Panda, P. Dash, J.-M. Yang and Y.-H. Chang, *Cellulose*, 2022, **29**, 2399–2411.
- 77 Z. Kalaycıoğlu, N. Kahya, V. Adımcılar, H. Kaygusuz, E. Torlak, G. Akin-Evingür and F. B. Erım, *European Polymer Journal*, 2020, **133**, 109777.
- 78 P. N. Manoudis, I. Karapanagiotis, A. Tsakalof, I. Zuburtikudis, B. Kolinkeová and C. Panayiotou, *Appl. Phys. A*, 2009, **97**, 351–360.
- 79 C. Esposito Corcione, N. De Simone, M. L. Santarelli and M. Frigione, *Progress in Organic Coatings*, 2017, **103**, 193–203.
- 80 C. Oleari, *Standard Colorimetry: Definitions, Algorithms and Software*, John Wiley & Sons, 2015.
- 81 J. K. McCormack, *Mineral. Deposita*, 2000, **35**, 796–798.
- 82 S. Pérez-Diez, A. Pitarch Martí, A. Giakoumaki, N. Prieto-Taboada, S. Fdez-Ortiz de Vallejuelo, A. Martellone, B. De Nigris, M. Osanna, J. M. Madariaga and M. Maguregui, *Anal. Chem.*, 2021, **93**, 15870–15877. DOI: 10.1039/D5NR02680F
- 83 M. K. Neiman, M. Balonis and I. Kakoulli, *Appl. Phys. A*, 2015, **121**, 915–938.
- 84 R. Nöller, *Studies in Conservation*, 2015, **60**, 79–87.
- 85 E. Gliozzo, *Archaeol Anthropol Sci*, 2021, **13**, 210.
- 86 W. Anaf, K. Janssens and K. De Wael, *Angewandte Chemie*, 2013, **125**, 12800–12803.
- 87 K. Keune and J. J. Boon, *Anal. Chem.*, 2005, **77**, 4742–4750.
- 88 M. Radepon, Y. Coquinot, K. Janssens, J.-J. Ezrati, W. de Nolf and M. Cotte, *J. Anal. At. Spectrom.*, 2015, **30**, 599–612.
- 89 K. Elert, M. Pérez Mendoza and C. Cardell, *Commun Chem*, 2021, **4**, 1–10.
- 90 J. Yu, W. S. Warren and M. C. Fischer, *Science Advances*, 2019, **5**, eaaw3136.
- 91 T. Hrbek, P. Kúš, M. G. Rodríguez, V. Matolín and I. Matolínová, *International Journal of Hydrogen Energy*, 2024, **57**, 187–197.
- 92 G. Wysecki and W. S. Stiles, *Color Science: Concepts and Methods, Quantitative Data and Formulas*, Wiley, 1967.
- 93 UNI 10921:2001 - UNI Ente Italiano di Normazione, <https://store.uni.com/uni-10921-2001>, (accessed October 16, 2024).
- 94 UNI EN 15803:2010 - UNI Ente Italiano di Normazione, <https://store.uni.com/uni-en-15803-2010>, (accessed October 16, 2024).
- 95 N. Fairley, V. Fernandez, M. Richard-Plouet, C. Guillot-Deudon, J. Walton, E. Smith, D. Flahaut, M. Greiner, M. Biesinger, S. Tougaard, D. Morgan and J. Baltrusaitis, *Applied Surface Science Advances*, 2021, **5**, 100112.



## Data availability

All data collected within this research is reported in the main text of the article and in its Supplementary Information. In the Supplementary Information file, additional data on the characterization of the nanoparticles and of the coating and additional information on the case study described are available.

